Ocean Engineering 319 (2025) 120135

Contents lists available at ScienceDirect

Ocean Engineering

journal homepage: www.elsevier.com/locate/oceaneng

Research paper

Experimental and numerical investigation of air lubrication on a planing hull with Double Interceptor System

Vincenzo Sorrentino, Riccardo Pigazzini *, Fabio De Luca, Simone Mancini, Claudio Pensa

Universita degli Studi di Napoli "Federico II", Dipartimento di Ingegneria Industriale, Italy

A R T I C L E I N F O

Keywords:
Experimental hydrodynamics
Computational fluid dynamics
Air lubrication
Planing hull
GHG emissions

A B S T R A C T

The present paper presents the study of the application of air lubrication system (ALS) on DIS (Double Interceptor System) equipped hull to improve its performances. It was observed that without ventilation, the low-pressure area behind the forward interceptor leads to excessive downforce, reducing trim and rise and increasing wetted surface with respect to the bare hull case. The air lubrication approach to improve the effectiveness of the DIS on a planing hull has been analyzed through natural and forced ventilation. The model has been tested for Fr between 0.97 and 1.46 (Fr_∇ between 0.67 and 0.94) and the air flow rate range was varied from 0 to 20.5 l/s.

The ventilated DIS showed significant improvements compared to non-ventilated DIS due to mutual effects between reduced wetted surface, pressure distribution and running attitude compared to the bare hull, the natural ventilation configuration showed improvements in resistance at lower speeds, but not enough to achieve substantial performance gains for higher speeds. Investigating the hull resistance and running attitude at different airflow rates, two key regions were identified, one where drag exhibits a significant decrease with airflow and a second one where only marginal reduction in resistance is obtained with increasing airflow.

1. Introduction

There is strong global attention to the study of the impact of anthropogenic activities on global warming. Mitigating climate change means reducing CO_2 and other greenhouse gas emissions, by undertaking large-scale actions that involve all stakeholders of the industry. Regarding the decarbonization of the shipping sector, the International Maritime Organization has adopted the 2023 IMO Strategy on Reduction of GHG emission (MPEC 80) (IMO, 2023). Different methodologies are available (with different Technology Readiness Levels) for cutting GHG emissions. Starting from the use of alternative fuels, the installation of devices for the reduction of propulsive losses to the use of renewable energy (*i.e.,* Flettner rotors, rigid sails, solar panels, *etc.*) one effective way is the adoption of direct drag reduction methodologies. Among these, Air Lubrication has gained widespread interest in the last decades.

The Air Lubrication System (ALS) reduces the ship's frictional drag by the injection of air beneath the hull bottom, spreading a continuous layer of bubbles or, for certain air flow rates forming a stable air layer between the hull and the water. From 2010 to 2022, more than 60 papers have already been published (Guedes Soares et al., 2023) on this topic. A comprehensive overview of the ALS state of the art is reported in (An et al., 2022), where different methodologies are described highlighting the leading factors, and the commonly used numerical models.

1.1. ALS methods

ALS can be classified into different methodologies according to the air injection mode and hull bottom configuration: Bubble Drag Reduction (BDR, or MBDR Micro-Bubble Drag Reduction), Air Layer Drag Reduction (ALDR), Air Cavity Drag Reduction (ACDR). Both BDR and ALDR systems share the same air injection mode (*ie*. porous panels or arrays of injection points), with different amounts of air flux injected in the near-wall boundary layer.

In BDR, the air is injected beneath the hull bottom as bubbles. The first experiments on drag reduction by means of micro-bubbles were conducted by (McCormick and Bhattacharyya, 1973) on a fully submerged 3-foot body of revolution. The hydrogen gas created by electrolysis reduced the viscous drag due to the alteration of the laminar and turbulent boundary layer properties. They observed that the amount of

* Corresponding author.
E-mail address: riccardovasco.pigazzini@unina.it (R. Pigazzini).

https://doi.org/10.1016/j.oceaneng.2024.120135
Received 8 July 2024; Received in revised form 12 December 2024; Accepted 14 December 2024
Available online 31 December 2024

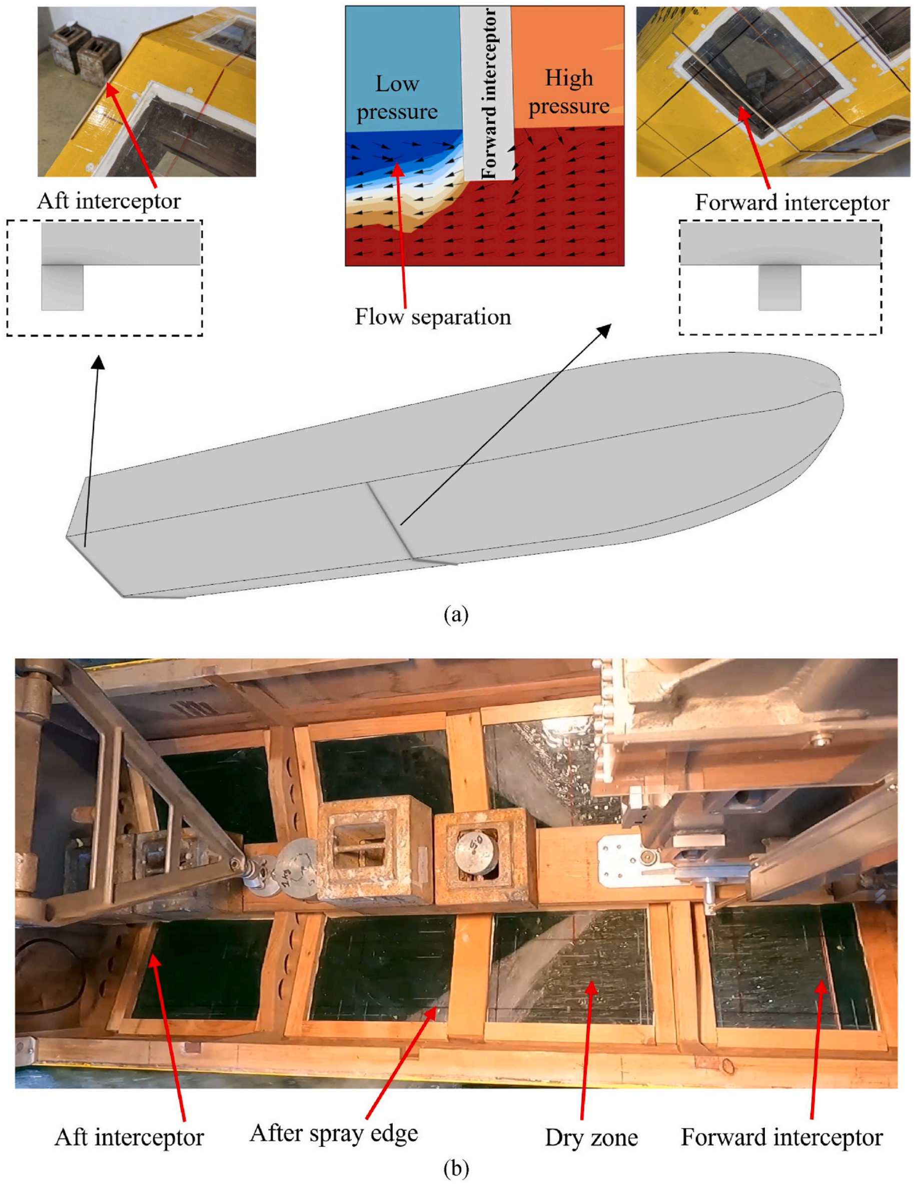

Fig. 1. (a) Prismatic planing hull equipped with DIS and interceptors centreline cross section details (b) DIS effect of the wetted surface distribution (from De Luca and Pensa, 2012).

Table 1
C1505 Model, hull details.

L_{WL} (m)	2.313
B_{WL} (m)	0.909
T (m)	0.157
∇ (m^3)	0.11
LCB (m)	0.867
S_W (m^2)	1.747
$L/\nabla^{1/3}$ (–)	4.823
L/B (–)	2.546
B/T (–)	5.804
LCG (m)	0.86
Forward interceptor longitudinal location (m)	1.09
Interceptor height (mm)	2.00

Table 2
Test cases of DIS-equipped hull and air flow rates.

Case	Air flow rate Q (l/s)
DIS No-air	0 (holes capped)
E8	5.57
G8	8.48
F8	9.69
C8	15.53
B8	20.47

viscous drag reduction depends on the free-stream speed and the produced hydrogen mass injected beneath the boundary layer. Years later, a series of microbubble experiments with circulating water tunnels followed (Kodama et al., 2002). measured the skin friction reduction by microbubbles in a circulating water tunnel for various speeds. They measured a maximum skin friction reduction of about 30%, with a greater effect for large air flow rates and lower speeds. In BDR mode, the drag reduction decreases with the downstream distance with respect to the injection holes Sanders et al. (2006); Tanaka et al. (2023), recently experimented with a repetitive bubble injection on a 36 m long flat-bottom ship model observing a higher drag reduction (24% at a towed speed of 8.0 m/s) with respect to the conventional continuous bubble injection.

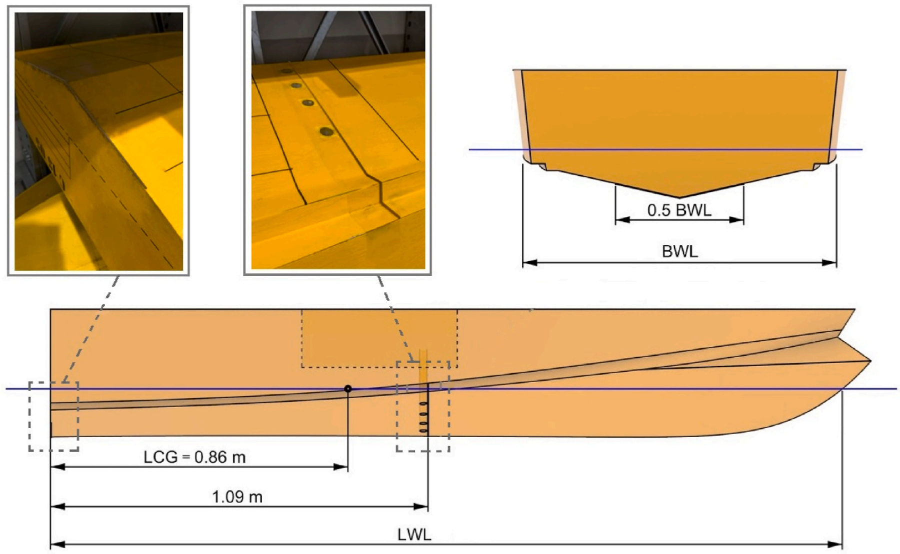

Fig. 2. C1505 Hull equipped with DIS and ventilation pipes (CAD file in supplementary material).

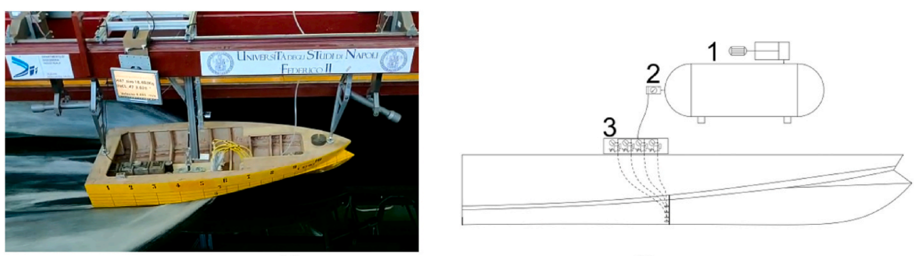

(a) (b)

Fig. 3. (a) C1505 model during tests, (b) scheme of the model air injection system: 1. High-pressure compressor/tank, 2. Pressure regulating valve, 3. High-impedance valve and manifold.

The ALDR requires larger air flow rates to obtain the bubble coalescence into a thin air layer detaching water from the hull bottom and reducing the wetted surface. When the air flux is increased, the micro-bubbles tend to coalesce in a continuous air layer and the ALDR condition can be obtained. Above a quantity of air flux, the stabilized air layer separates the wall surface from the free-stream liquid leading to friction reduction (Elbing et al., 2008). investigated the transition between BDR and ALDR on a flat-plate test model at large scales and high Reynolds numbers. Based on air injection rate, three different regions can be distinguished: a BDR regime with linear drag reduction, a transitional zone with still a linear increasing trendline, but with a much steeper slope and a fully developed ALDR regime where nearly 90% of drag reduction is observed. They found a 'critical' injection rate proportional to the square of the free-stream flow above which no significant drag reduction is observed. Based on the experimental data reported by Elbing (Wang et al., 2010), validated URANS simulations of the ALDR development on a large-scale flat plate. They achieved a significant drag reduction in the ALDR mode showing good agreement with experimental data. The transitional regime between BDR and ALDR was obtained with a lower critical air flow rate than in the experiments.

In ACDR, the air layer is confined in a ventilated cavity made from a shallow hull recess.

In the ACDR the friction drag reduction can be achieved if a stable air layer covers a considerable cavity portion. Initial pioneer systematic research on air cavity ships, was initiated by (Butuzov, 1966). An aspect to consider when designing air cavity ships is the cavity length defined as the length of the developed air pocket in the cavity recess. The cavity length is proportional to the square of the ship speed and depends on the recess geometry, the wavelength and flow pressures. The combination of these parameters that optimize the cavity length (i.e. a stable air cavity form with no pulsating re-entrant water jets) is called "limiting parameters" (Matveev, 2003). (Matveev et al., 2009; Butuzov, 1966) suggested a linearized potential-flow approach to predict the limiting cavity length highlighting its dependence on wavelength. The ACDR is applicable to a wide variety of ship hulls.

1.2. ALS for planing hulls

Regarding the application of ALS for planing hulls, the ACDR method takes advantage of low-pressure regions developed behind the backwards-facing steps, typically found on stepped planing hulls (Vitiello et al., 2022), (Ricks et al., 2023). (Latorre, 1997) made a historical overview of the first bottom air injection systems, already implemented on planing hulls before the First World War. Later (Latorre et al., 2002) conducted model and full-scale tests on high-speed craft using a 2.3 m model and a 16.6 m catamaran demonstrator. With the MBDR system switched on, they obtained a 10–15% resistance reduction on model tests and a 2.5–3% speed increase at 40–45 knots during full-scale trials (Collins et al., 2021). performed experimental and numerical tests of a boat equipped with an air cavity, in a range of speed between Fr = 0.17 and 0.5, observing the influence on cavity length and drag reduction by varying load conditions and speed. Then they compared the experimental data with numerical simulation using the VOF method and two different mesh approaches.

(Wang et al., 2020) conduct an extensive experimental campaign on the growing behavior of a ventilated ship model. They observed several

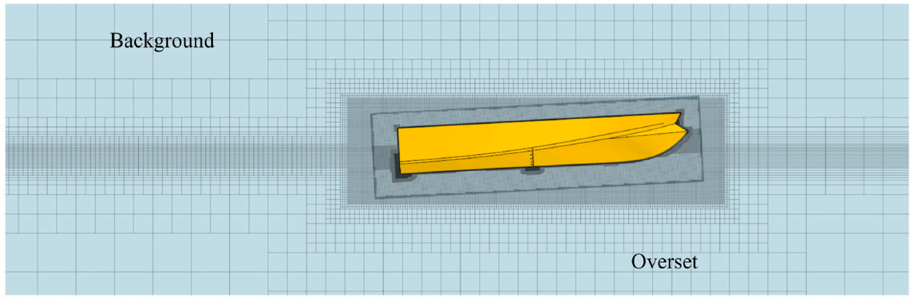

(a)

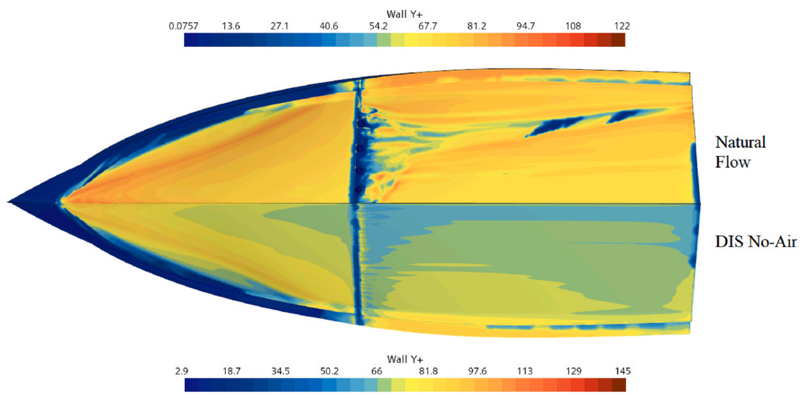

(b)

Fig. 4. (a) Background and overset region, (b) Wall y + for natural flow case (up) and DIS No-Air (down).

Table 3
Numerical and solver setup.

solver	Implicit unsteady
Convection term	2nd order
Turbulence model	k-Omega SST
Time step (s)	$\Delta t < 0.01 \frac{L_{wl}}{v}$
Temporal Discretization	1st order
Iteration per time step	10
Mesh motion	Overset
Overset Interpolation scheme	Linear
Wall treatment	All y + wall treatment

distinct cavity patterns based on flow rate and Froude Number. Later (Fang et al., 2021, 2023), extended the study with RANS-VOF simulations, evaluating the dependence of flow rate on drag reductions and the influence on heeling stability. They found a skin friction reduction of 40% determined by the cavity wetted surface reduction and an influence of flow rate on cavity pressure distribution leading to higher dynamic hull rises and a reduced trim compared to the unventilated cavity baseline. Further ALS can be introduced by considering the use of devices such as hydrofoils and non-common interceptor systems (Kumagai et al., 2015). tested the BDR using a power-saving device based on an air-assisted angled hydrofoil. They carried out full-scale tests on four different types of ships, obtaining a net power saving of 5–15%. An example of ALS combined with non-common interceptor systems is the ventilated Double Interceptor System (DIS). The DIS is a high lift device used as a trim corrector at high speeds pair of interceptors placed one at the transom and one forward (De Luca and Pensa, 2012a,b). The flow deviation provided by the forward interceptor determines a low-pressure zone that triggers natural ventilation by drawing the air from the hull sides. Therefore, the dry zone developed behind the forward interceptor reduces the wetted surface. The application of a DIS-based ALS requires considerable attention because of possible instability phenomena at high speed and ventilation issues (De Luca and Pensa, 2012). Regarding ventilation issues, in specific hull geometries with a low slenderness ratio or in heavy-loaded conditions, the DIS may be unable to trigger ventilation. In the case of such hull forms, a solution has been proposed by (De Luca et al., 2022), using dedicated air ventilation pipes placed behind the forward interceptor to assist the ventilation, experimental and numerical tests were performed with different air flow rates showing a notable improvement of the DIS effectiveness. This solution has been further extended by (De Luca et al., 2023a,b) performing full-scale CFD simulations to assess full-scale performances and highlight possible scale effects. Furthermore, a scaling law has been proposed for the scaling of the air flow rate to improve model-ship correlation methodologies for DIS-equipped air lubricated planing hulls.

1.3. Scope of work

The present work is an extensive experimental and numerical study on the application of ALS on DIS-equipped hulls using dedicated air ventilation pipes, to improve the performances on specific hull forms and speed ranges where the DIS is not effective. In this study, the *C1505* model has been adopted (CAD file is available in supplementary material), for which the experiments in the towing tank with DIS have highlighted serious ventilation issues. The DIS performances have been investigated with two different ventilation approaches.

- Natural ventilation, where the ventilation pipes, placed on the low-pressure zone downstream of the forward interceptor, are open to the atmosphere
- Forced ventilation, using a systematic air flow rate variation through the same pipes

The results of the experimental and numerical tests have been analyzed and compared to the bare-hull condition (hull without DIS) and the non-ventilated condition (DIS-equipped hull without ventilation

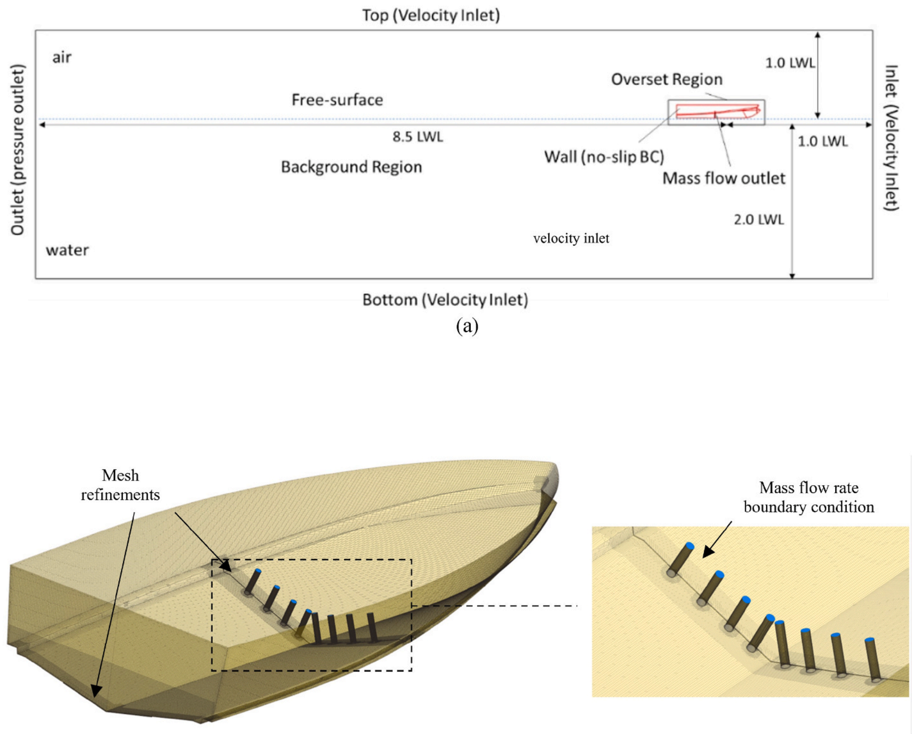

Fig. 5. (a) Computational domain and boundary conditions, (b) Pipes arrangement and boundary condition details.

Table 4
Boundary conditions.

Boundary	Type
Hull surface	No-slip wall
Inlet, Top, Bottom, Sidewall	Velocity inlet
Outlet	Pressure outlet
Symmetry	Symmetry plane
Pipes inlet	Mass flow inlet

pipes).

The paper has been organized as follows: in the first part (Section 2) the DIS has been introduced to provide a general overview of its working principles. The experimental and numerical setup are provided in Sections 3 and 4. The results and conclusions of the study are discussed in Sections 5 and 6. An appendix containing the numerical-experimental comparisons and underwater photos of the towing tank tests were included.

2. The Double interceptor system

The *Double Interceptors System* (DIS) solution, proposed by (De Luca and Pensa, 2012a,b) consists of two interceptors (Fig. 1 (a)), where one interceptor is placed at the transom, as usual, and a second one forward. The DIS aims to limit the excessive trim correction of the transom interceptor at high speeds by providing additional bow-up pitching moments through the high pressure (and thus lift) generated by the forward interceptor (Fig. 1 (a)), Moreover, the forward interceptor provides a sizeable dry zone on the hull surface downstream provided by the flow detachment (Fig. 1 (b)), reducing the total wetted surface and thus the hull skin friction. In Fig. 1 (a) the typical placement of DIS, along with the interceptors' longitudinal cross-sections are shown. In addition, a schematic working principle of the forward interceptor is provided for clarity.

The main difference between the DIS and other wetted surface reduction methodologies such as air injection and stepped hulls resides in the fact that the dry zone is provided by flow deflection instead of hull discontinuity, thus providing a high-pressure and lift zone forward of the detachment.

Although the effectiveness of the DIS is very promising, the resistance reduction provided by the system is dependent on the hull geometry. In this regard, the range of applications of this system needs an in-depth investigation, since, in addition to possible performance degradation, it has been shown that it can lead to dynamic instability phenomena at high speeds (De Luca and Pensa, 2012b).

3. Experimental setup

The model experiments have been carried out at the LEIN towing tank at the *Università degli Studi di Napoli "Federico II"*. The towing tank is 136.0 m long, 9.0 m wide and 4.5 m deep and the carriage has a maximum speed of 10.0 m/s.

The *C1505* model used in the present study is a planing hull designed as a workboat in confined waters with search and rescue capabilities. The main dimensions and coefficients of the model are shown in Table 1. As it can be observed, according to the operational requirements the C1505 is a heavy load hull characterized by a low L/B ratio (broader hull for transversal stability) and $L/\nabla^{1/3}$.

The experimental restraints were set up to provide free trim and pitch through a cardan joint at the hull CG (center of gravity), together with vertical guides at the bow and aft to restrain yaw motion. Due to the high speed involved ($Re > 1.0 \times 10^7$) in the tests, together with the presence of the DIS, no turbulence stimulators were used for the experiments. The model's mass configuration used for the experiments led to a static trim of 0.6 deg forward. The model has been tested at speeds 4.60, 5.52, 6.44, and 6.90 m/s, corresponding to Froude numbers between 0.97 and 1.46 (Fr_∇ between 0.67 and 0.94).

Forced air injection (Fig. 3 (b)) was provided through a high-pressure

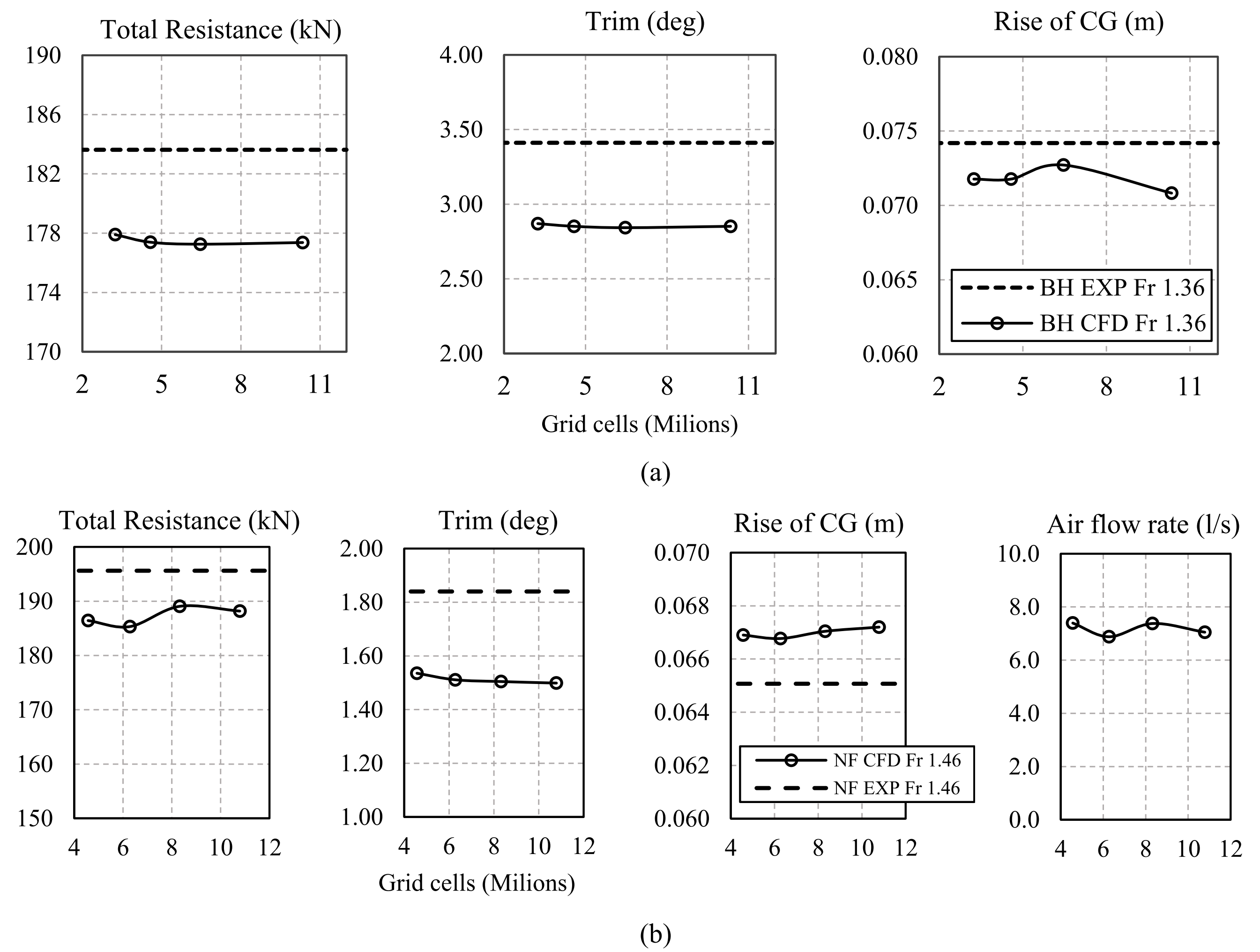

Fig. 6. Grid independence analysis (a) Bare Hull case at Fr = 1.36, (b) Natural Ventilation at Fr = 1.46.

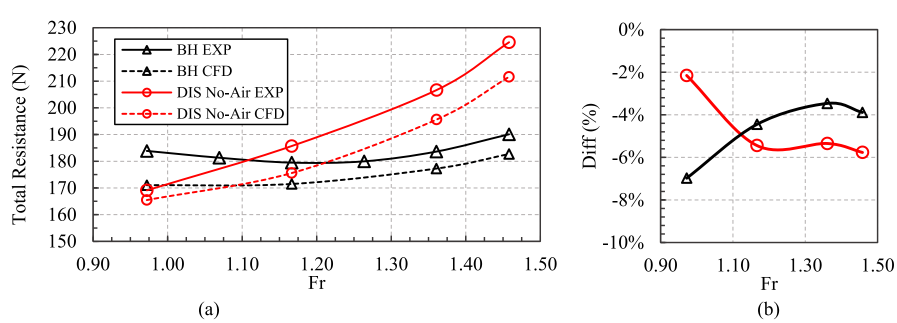

Fig. 7. (a) Experimental and numerical total resistance of the Bare-Hull and DIS No-Air cases vs speed. (b) Differences in percentage between experimental and numerical total resistance.

compressor and tank connected to a pressure regulating valve, together with high impedance valves at the on-board manifold, just before the injection ports to ensure constant flow regardless of the bottom pressure variations. The forced mass flows were calibrated in advance and correlated to the output pressures of the regulating valve. The dynamic of the air cavity and the effects on hull performances and attitude have been studied by systematically increasing the air flow rates, from zero to 20.5 l/s (see Table 2).

The hull has been tested with eight air injection pipes with a diameter of 20 mm each, placed at 45, 108, 184 and 270 mm from the centerline, 1080 mm from the transom stern, just behind the forward interceptor. The hull equipped with the interceptors and the ventilation pipes is shown in Fig. 2. The height of the interceptors is 2 mm, the stern interceptor width is $B_{WL}/2$, and the forward interceptor is placed at 10% L_{WL} forward of the center of gravity (Fig. 2). The forced air flow rates were experimentally measured with the stationary hull outside the towing tank by a propeller-based flow meter.

The natural airflow rates (NF) are estimated by means of CFD simulations, where the hull has been simulated with the eight pipes open to the atmospheric pressure. Natural airflow rate measurements were not

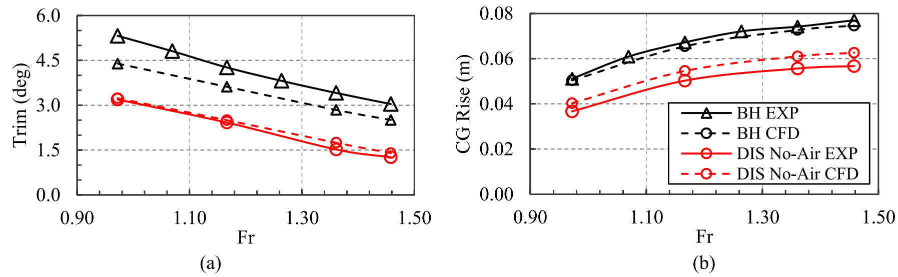

Fig. 8. (a) Trim and (b) rise of CG vs speed (Experimental results).

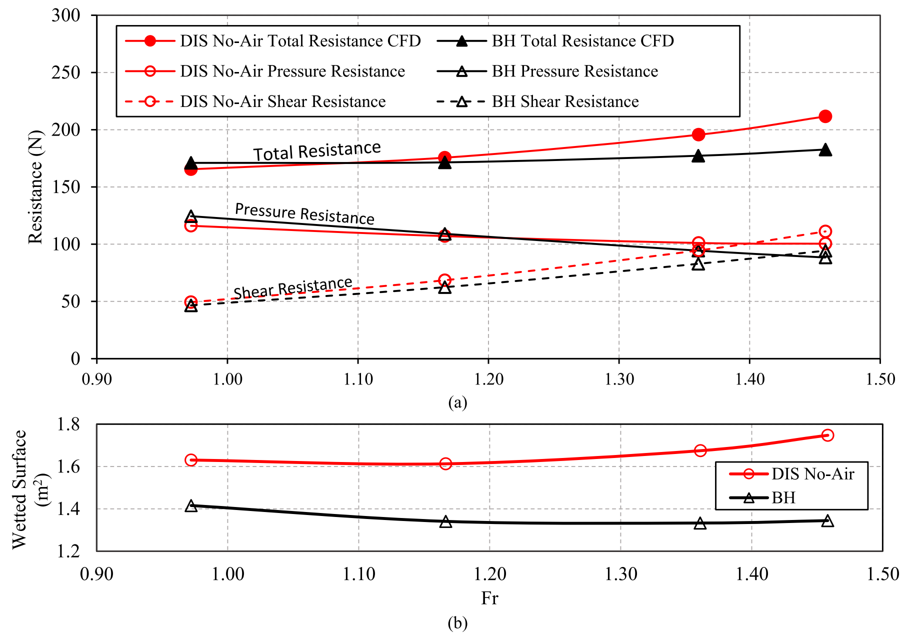

Fig. 9. (a) Shear (dotted curves) and Pressure (continuous curves) resistance components vs speed (CFD data) (b) Wetted surface vs speed (CFD data).

reliable as the available measurement system was not suitable for on-board measurements during the experiments.

4. Numerical setup

In this study, Computational Fluid Dynamics (CFD) simulations were conducted using the commercial software, Siemens PLM Star CCM+ version 2022.1.1. The fluid motions are modeled with Unsteady RANS (Reynolds-averaged Navier-Stokes) based approach. The Overset/Chimera mesh was employed in the simulations requiring the implementation of two regions: background and overset regions, Fig. 4 (a). The connection between these two computational regions is established with a linear interpolation scheme, as suggested by (De Luca et al., 2016).

The segregated flow was solved using the Semi-Implicit Method for Pressure-Linked Equations (SIMPLE) algorithm, which is a commonly used algorithm for coupling pressure and velocity fields. To enhance the convergence speed and accuracy of the simulations, an Algebraic Multi-Grid (AMG) solver was employed. Furthermore, to accurately capture and model the free surface of the fluid flow, a two-phase Volume of Fluid (VOF) approach was utilized. This method tracks the interface between the air and water using a High-Resolution Interface Capturing (HRIC) scheme based on the Compressive Interface Capturing Scheme for Arbitrary Mesh (CICSAM). The k-Omega SST turbulence model has been utilized to incorporate turbulence influences in the flow.

In addition to these techniques, the wall treatment has been addressed by implementing the All-Wall y + approach. This approach is a hybrid strategy that uses a combination of fully resolved boundary layer velocity distribution (i.e. typical of low-y+, also called low-Reynolds, approach) and fully wall function (also called high y + approach) to resolve near-wall flow behavior. The wall y + values on the hull for two significant cases (natural flow and DIS No-Air) are shown in Fig. 4 (b). For more details on the All-wall y + approach, refer to the Siemens PLM Star-CCM + v. 2022.1.1 User's Guide (Siemens, 2022).

The time step is determined using the ITTC 7.5-03-02-03 suggestion (International Towing Tank Conference ITTC, 2014), which recommends a time step below 0.01 times the characteristic length divided by the velocity.

As an overall recap, all the main solver setup is summarized in Table 3.

The dimensions of the computational domain used in these simulations were based on the ITTC 7.5-03-02-03 guideline (ITTC, 2014).

The boundary conditions applied are detailed in Fig. 5 (a) and Table 4. The boundary conditions are the standard for typical hull towing simulations. However, since the focus of this study was to evaluate the performance of natural ventilation, an additional boundary condition was set at each pipe inlet (as shown in Fig. 5 (b)) to ensure a determined flow rate for the forced ventilation system. In cases where natural ventilation was being evaluated, no forced flow boundary conditions were imposed, and the mass flow was measured at the pipe outlets. Each inlet was left open to atmospheric pressure.

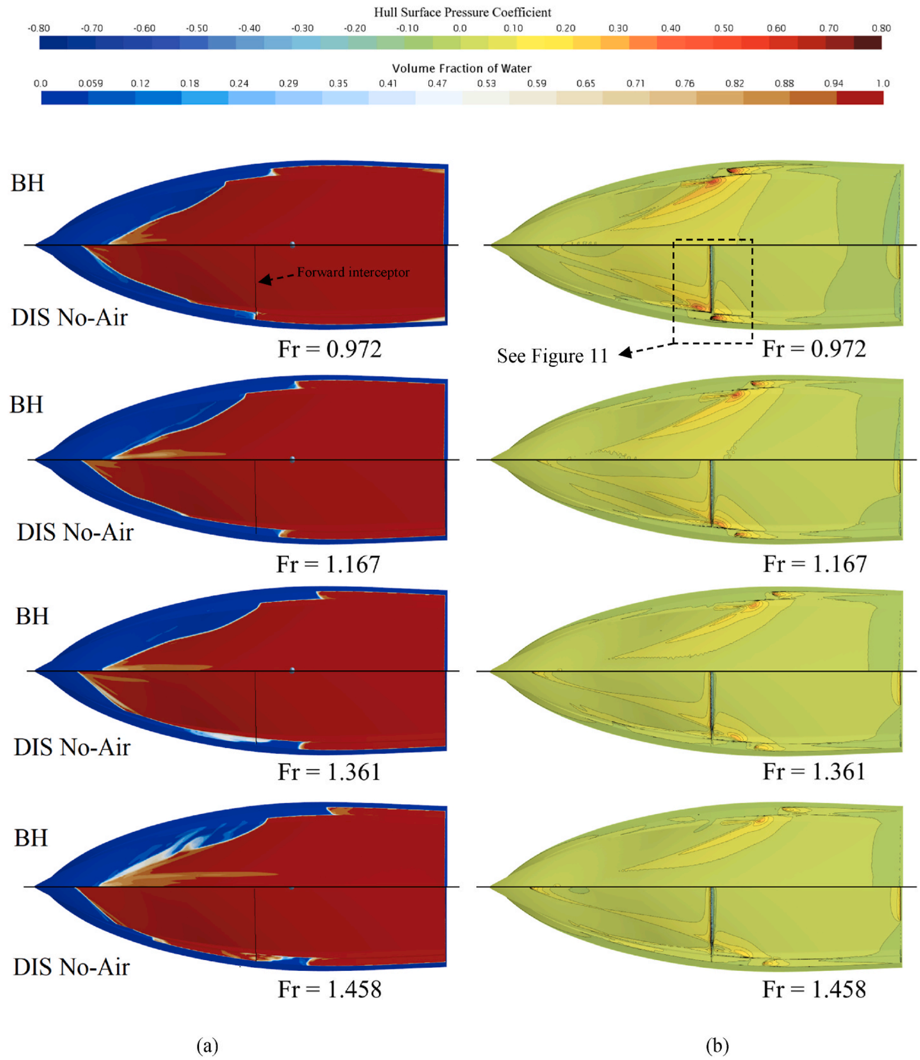

Fig. 10. (a) VOF for the BH and No-Air conditions (b) Hydrodynamic pressure coefficient for the BH and No-Air conditions.

4.1. Grid independence analysis

It is well known that one of the main sources of uncertainty in the numerical simulation of planning hulls is related to the mesh (e.g. Stern et al., 2001; De Luca et al., 2016). Therefore, it is crucial to assess the dependency of the simulation results on the grid. This involves analyzing the impact of different grid resolutions on the numerical results. To address this, a thorough grid independence analysis was conducted for the bare hull case at a speed of 6.44 m/s (Fr = 1.36) and for the hull equipped with DIS in natural ventilation mode at the speed of 6.90 m/s (Fr = 1.46). This analysis involved using different grid resolutions and comparing their corresponding results. The findings were then compared to the experimental results. The results of this analysis are presented graphically in Fig. 6.

From the plots in Fig. 6 (a), there is substantial independence of the results from the grid size, particularly for the resistance and dynamic trim, for grid resolutions above 5 million cells. In terms of the rise of CG, the observed trend is not strictly asymptotic, but the range of oscillation in absolute value is significantly small.

In conclusion, for the Bare Hull case, a grid resolution with more than 5 million cells provides accurate results for further simulations.

Regarding the mesh independence study for the DIS in natural ventilation (Fig. 6 (b)), a convergent trend was detected for the dynamic trim and rise of CG. Instead, an oscillatory convergent trend was detected for the resistance. Furthermore, for the natural ventilation case, the air flow rate has been included in the mesh independence analysis as well and, similarly to the resistance, an oscillatory convergent trend was observed. Anyway, for a grid size above the 8 million cells, the results appear to be less dependent on the grid size.

For the latter and for the other ventilated cases, a grid resolution of more than 8 million has been adopted.

5. Results and discussion

To provide a better insight into the phenomena under investigation, the results paragraph is organized as follows.

- Section 5.1 reports the bare hull (BH) and non-ventilated DIS (DIS No-Air) experimental and numerical results, in terms of resistance, rise of CG and trim.
- In section 5.2, cases related to the ventilated DIS are discussed. The results are supported by experimental evidence and numerical results. Finally, resistance reductions of all ventilated cases, in comparison to the bare hull, are shown.
- In section 5.3, the experimental and numerical results regarding the DIS-equipped hull are presented through iso-speed plots to highlight the influence of the variable air flow rate on total resistance and running attitude. Moreover, the growth of the air layer as the air flow varies is described showing the vector plots obtained from CFD simulations.

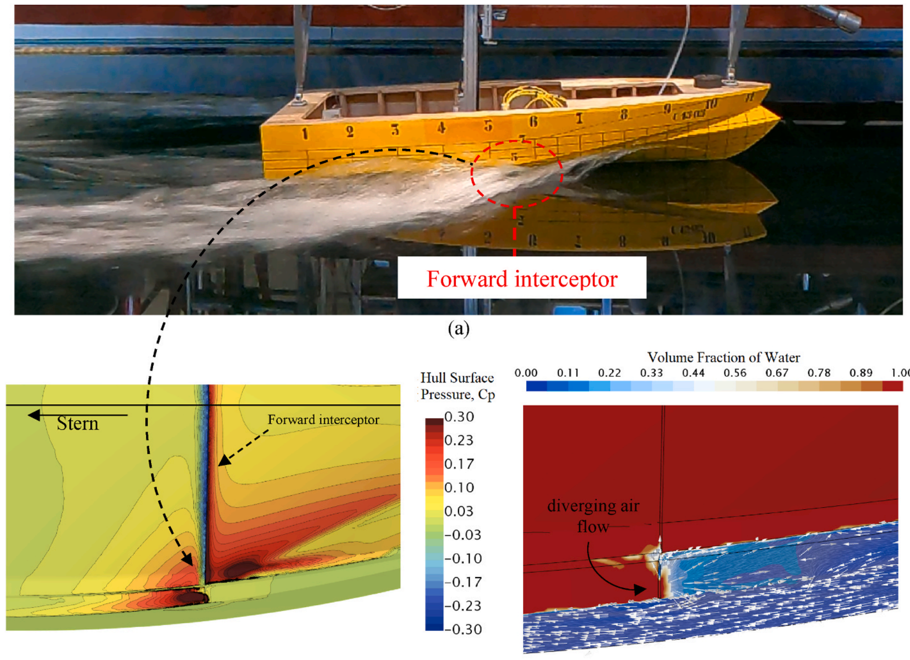

Fig. 11. (a) The hull in DIS No-Air condition during tests at Fr = 0.972, (b) Detail of the hydrodynamic pressure distribution near (c) VOF and air flow vector field (white arrows).

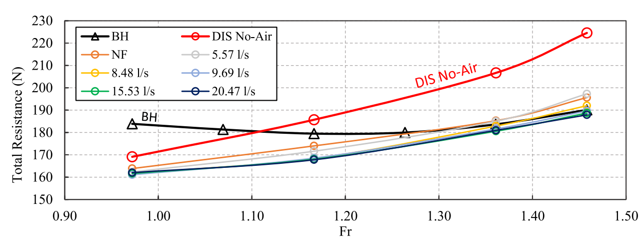

Fig. 12. Total resistance vs speed, all cases (Experimental results).

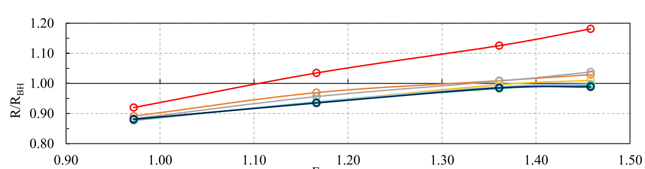

Fig. 13. Total resistance reduction ratios $\frac{R}{R_{BH}}$ vs speed (Experimental results).

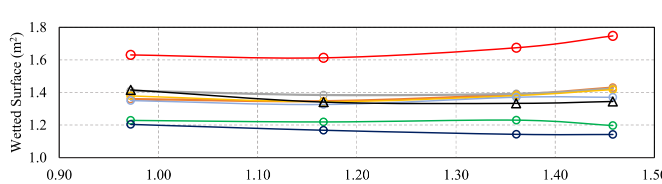

Fig. 14. Wetted surface vs speed, all cases (CFD results).

5.1. The non-ventilated DIS

Here we analyze and compare the cases of Bare Hull (BH) and non-ventilated DIS in order to provide a baseline for the ventilated DIS case results.

The analysis has been carried out with experimental and numerical tests. An overview of the experimental and numerical comparisons is provided in Fig. 7 (a) for the BH and DIS No-Air cases, in Fig. 7 (b) the differences in percentage are highlighted showing acceptable comparison errors for main parameters at the simulated speeds (International Towing Tank Conference ITTC, 2014). For all tested cases, the comparisons between numerical and experimental results, including hull running attitude have been provided in reference Appendix A.

The trim reduction provided by the DIS (Fig. 8 (a)) is due to the absence of ventilation on the forward interceptor, resulting in its ineffectiveness. The resulting trim reduction increases the total resistance, as shown in Fig. 7 (a), as in the case of a single stern interceptor. The absence of ventilation reduces the CG rise with respect to the BH case Fig. 8 (b). This counterintuitive behavior is explained by observing that the high-lift effect of the forward interceptor is not enough to counterbalance the downforce generated by the low-pressure area immediately behind the interceptor (Fig. 11(a)).

To further investigate the differences seen between the experimental results of the two cases, simulations were carried out to provide a detailed assessment of the hydrodynamics phenomena involved. CFD results allow for analysis of the pressure and shear components of the total resistance. In Fig. 9 (a) the resistance components for BH (black curves) and DIS No-Air (red curves) cases are shown. The following aspects can be highlighted.

- At lower speeds (Fr = 0.972), there is a slightly higher pressure resistance for BH than the DIS No-Air, determined by the higher trim (consistent with the experimental evidence discussed above). As the speed increases, the relative position of the curves is inverted and the difference increases. It is worth noting that even if the DIS No-Air case shows lower running trim, the pressure resistance components increase, due to the over-submerging of the bow.
- Although the difference in shear resistance at lower speeds is minimal (Fig. 9 (a)), the DIS No-Air case shows a bigger wetted surface with respect to the BH case (Fig. 9 (b)). The increased wetted area is

Table 5
Experimental resistance reductions and increments in % respect bare-hull (-reductions, + increments).

Fr	No-Air	nf	5.57 l/s	8.48 l/s	9.69 l/s	15.53 l/s	20.47 l/s
0.972	−8.0%	−10.9%	−11.7%	−12.1%	−12.4%	−12.1%	−11.9%
1.167	+3.5%	−3.1%	−4.4%	−6.2%	−6.1%	−6.4%	−6.5%
1.361	+12.6%	+0.9%	+0.8%	−0.4%	−1.1%	−1.7%	−1.5%
1.458	+18.1%	+2.9%	+3.8%	+1.0%	−0.2%	−0.7%	−1.2%

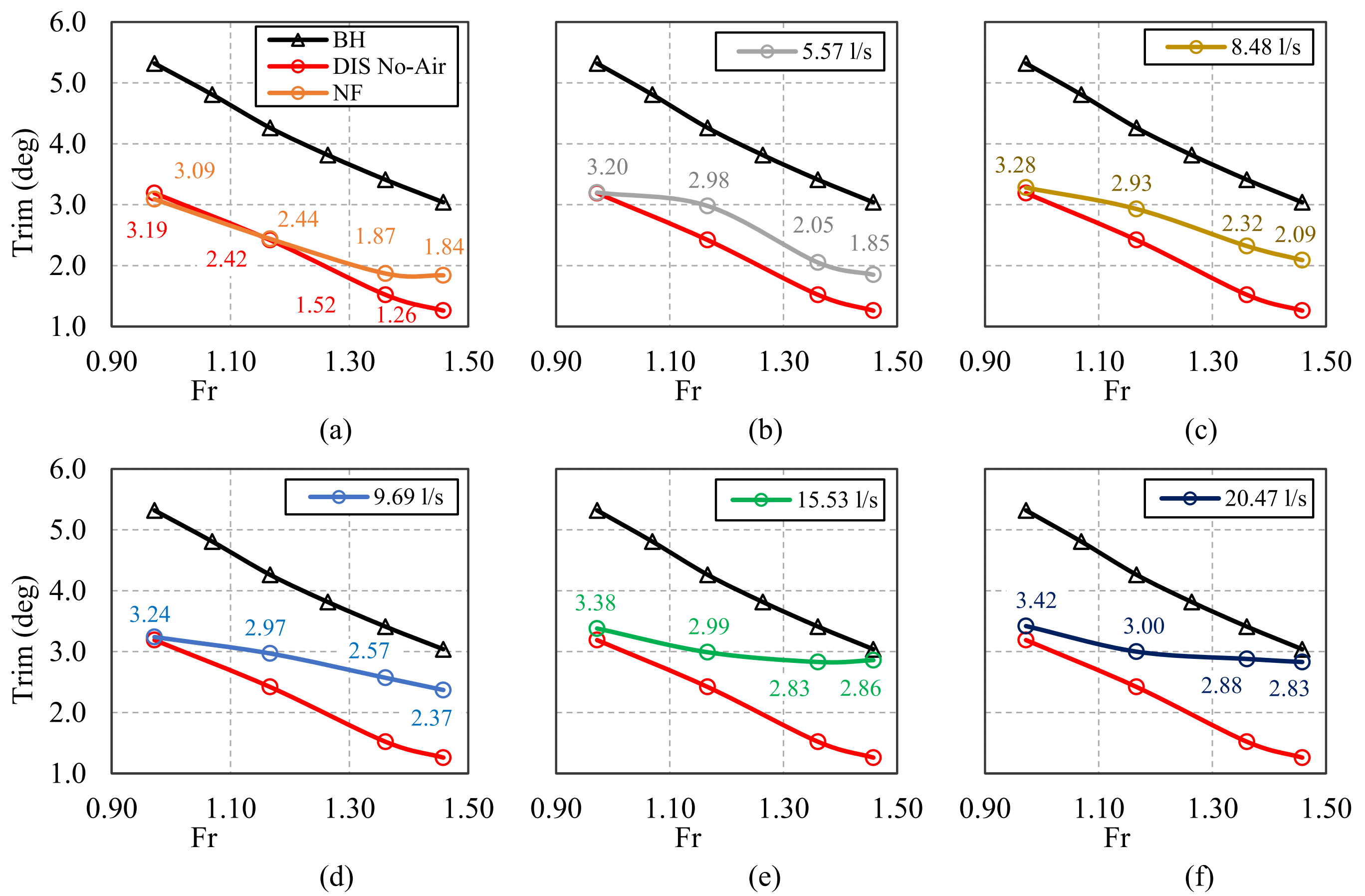

Fig. 15. Dynamic trim vs speed for all tested cases (Experimental results). The dynamic trim related to Bare-Hull and No-Air cases is repeated in each plot to highlight the effects of forced ventilation on dynamic trim.

due to the low-pressure zone developing behind the forward interceptor, leading to lower trim values (Fig. 8(a)).

- Moreover, wetted surface curves diverge from Fr = 1.167 upwards increasing the difference in shear resistance between the two cases.

Based on the previous observations on the resistance components, it can be concluded that at higher speeds, the added wetted surface of the non-ventilated DIS provides for a notable increase in the shear resistance component and the pressure resistance due to the interceptors, outweighing the beneficial effects of a lower running trim.

Fig. 10 (a) shows the volume fraction of water for the BH and No-Air cases as a function of hull speed. In the case of DIS No-Air, the larger wetted surface (due to both lower running trim and rise of CG with respect to the BH case) is clearly visible. Moreover, for higher speeds the hull chines tend to get wet, leading to a further increase in wetted surface.

Fig. 10 (b) compares the hull bottom dynamic pressure coefficient distribution for the two cases. The dynamic pressures generated by the non-ventilated DIS, Fig. 10 shows a fully wetted hull bottom and a marked low-pressure zone behind the forward interceptor that strongly reduces the expected lifting effect provided by the interceptors. Consistently, the dynamic pressure distribution given by the forward interceptor increases the bow-down effect of the stern interceptor.

The photo of the hull in DIS No-Air condition at Fr = 0.972 and the corresponding representation of the dynamic pressure distribution near the forward interceptor is provided in Fig. 11(a and b), where it can be observed that high-pressure areas are determined by the stagnation flow over the chines. As can be seen in the air vector field shown in Fig. 11 (c), the high-pressure areas over the chines block the airflow, leading to the absence of ventilation behind the forward interceptor.

In this section, the shortcomings of the non-ventilated DIS have been highlighted, the absence of ventilation behind the forward interceptor strongly inhibits its high lifting characteristics and increases the overall wetted surface resulting in poor performances, especially at high speed, where the effect of the wetted bow geometry becomes relevant.

5.2. *The ventilated DIS*

Given the observations made regarding the non-ventilated DIS and its inability to deliver performance improvement in this case study, eight

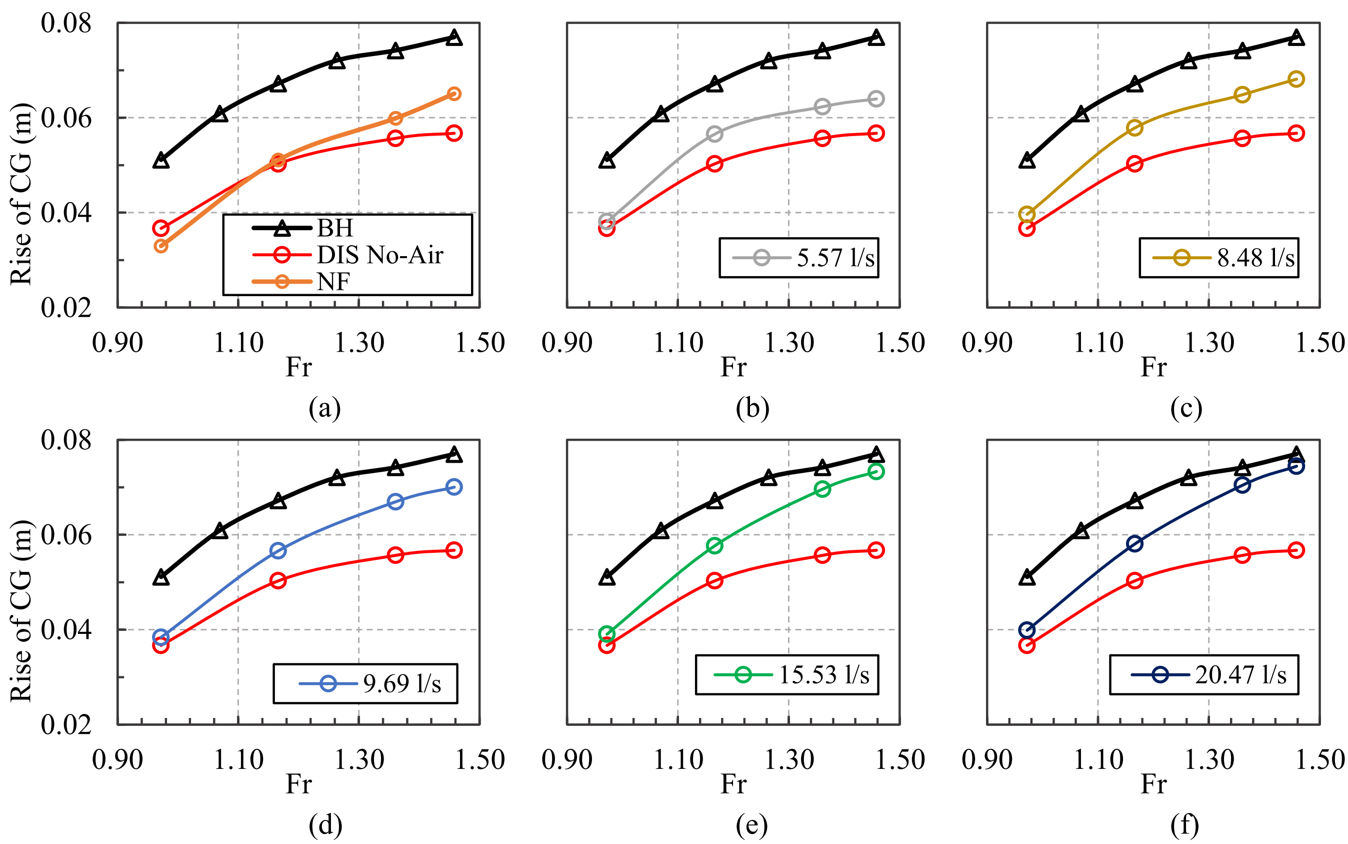

Fig. 16. Rise of CG vs speed for all tested cases (Experimental results).

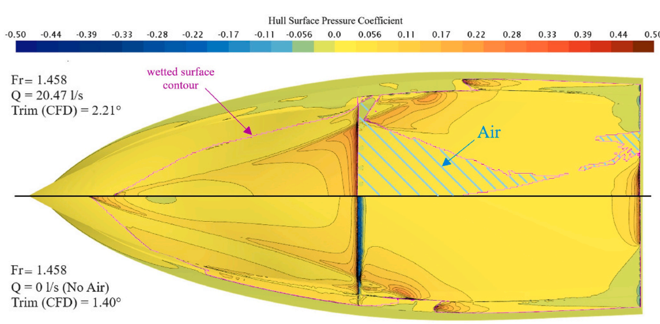

Fig. 17. Hull bottom pressure distribution comparison, wetted surface outline in magenta.

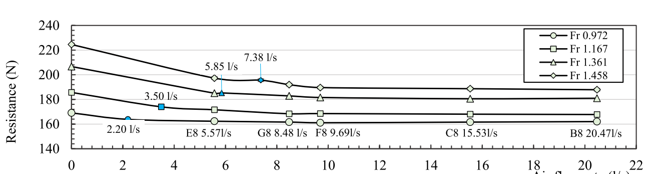

Fig. 18. Resistance vs air flow rate for different tested speeds (Experimental results, NF air flow rates calculated by CFD natural flow simulations).

ventilation pipes were installed to enhance its performance. The pipe outlets are located just behind the forward interceptor, taking advantage of the low-pressure zone (Fig. 10 (b)) generated by the flow detachment.

The plot presented in Fig. 12 shows the results of the experimental tests for the ventilated DIS. The "NF" (orange curve) case refers to the natural flow condition, where the upper end of the pipes is open, and

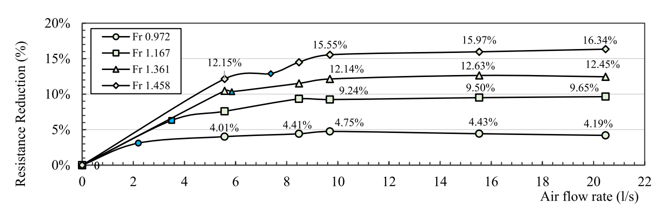

Fig. 19. Resistance reduction respect DIS No-Air in percentage vs air flow rate (Experimental results).

airflow is provided by the pressure gradient between atmospheric pressure and the downstream zone of the forward interceptor, minus the pipes' pressure drop. The other cases (E8 to B8: Q = 5.57–20.47 l/s) refer to forced ventilation conditions, where the air injection system provides a given volumetric flow using the setup described in Section 3.

From the plot, it can be clearly seen that for all ventilated cases there is a notable improvement with respect to DIS No-Air (red curve), at higher speeds. Resistance reduction with respect to the bare hull is also achieved, although at higher speeds only the higher airflows are effective (9.69 l/s, 15.53 l/s and 20.47 l/s). In Fig. 14, the wetted surface area for all ventilated cases is reported, obtained from CFD simulations. Consistently with the resistance improvements, a significant reduction of the wetted surface area is observed when compared to the DIS No-Air case, especially for cases with high air flow rate.

To highlight the resistance reduction capabilities of the ventilated DIS with respect to the BH case, the ratio R/R_{BH} has been calculated in Fig. 13. The ratios in terms of resistance reductions and increments with respect to BH are also reported as colour-coded percentages in Table 5, the maximum resistance reduction at low speed (Fr = 0.972) is 12.4% for 9.69 l/s case, while for high speed the higher air flow rate is required, with a resistance reduction 1.7% at Fr = 1.361 (15.53 l/s) and 1.2% at

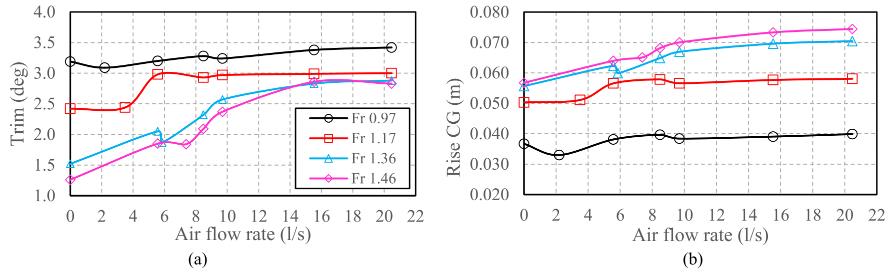

Fig. 20. (a) Trim vs air flow rate, (b) Rise of CG vs air flow rate (Experimental results).

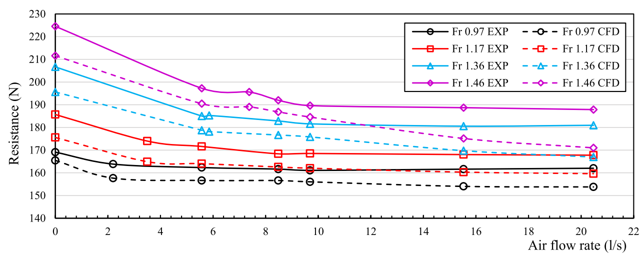

Fig. 21. Comparison between experimental (solid curves) and numerical (dotted curves) total resistance results.

Fr = 1.458 (20.47 l/s). A maximum resistance increment of 3.8% respect BH has been obtained at high speed (Fr = 1.458) for the minimum forced air flow rate (5.57 l/s).

The plots in Figs. 15 and 16 show the hull experimental running attitudes for all ventilated cases. In each plot, the running attitude (dynamic trim and CG rise) related to BH and DIS No-Air cases is reported to highlight and evaluate the effects of forced ventilation. As the air flow rate increases, differences in running trim and rise of CG increase with hull speed (curves relative to forced ventilation cases diverge). The lifting effect of the higher airflow cases (15.53 l/s and 20.47 l/s) can be observed in the plots (e), and (f) in Fig. 15, as the running trim trends at high speed (Fr > 1.15) are flatter, and trim is higher than the lower airflow cases. The lifting effect also results in an increased rise of CG values at higher speeds (Fig. 16(e) and (f)).

The effect of the injected air on the hull bottom pressure distribution is shown in Fig. 17 for the highest speed and flow rate. It can be shown that when the forward interceptor is ventilated, the pressure distribution changes dramatically. In particular, the non-ventilated DIS shows a strong depression downstream of the forward interceptor, leading to a downforce ahead of the CG. When the DIS is ventilated, the low-pressure zone behind the forward interceptor disappears and a large high-pressure zone upstream is developed. This provides an increased running trim and rise of CG. It is worth noting that the increased running trim also leads to higher dynamic pressure on the bow hull surface.

Moreover, at high speed, the running attitude is similar to the BH case for medium-high air flow rates (9.69 and 15.53 l/s), and the resistance trend tends to the BH case, with comparable resistance values (a minimum resistance reduction of 0.2% respect BH has been observed).

In this section, the effects of the ventilation downstream of the forward interceptor are investigated in terms of resistance, wetted surface and running attitude by comparing the experimental and numerical results with the non-ventilated cases. The results showed that the differences with the non-ventilated case increase with hull speed, if the bare hull case is considered the contrary is valid. Numerical results show that when the DIS is ventilated, the low pressure behind the forward interceptor disappears and a large high-pressure zone upstream is developed, enabling the working principle of the high-lift device.

5.3. Air layer dynamics

In this section, the focus is on the analysis of the ventilated cases, in particular highlighting the effects of the air flow rate on both running attitude and resistance. In addition, some considerations on the air layer development and morphology are proposed. To analyze the effects of an increasing flow rate on DIS performances, the experimental results have been presented as a function of the air flow rate at different speeds. The plot presented in Fig. 18 shows experimental resistance curves for the DIS-equipped hull starting from the non-ventilated condition (DIS No-Air) to the maximum forced ventilation (Q = 20.47 l/s). The plot in Fig. 19 shows the drag reduction calculated with respect to the non-ventilated DIS condition (Q = 0.0 l/s).

Since the natural ventilation is triggered by the low-pressure area behind the forward interceptor, the resulting flow rate depends on the hull speed. Hence, at lower speeds (Fr = 0.972, 1.167), the natural air flow rate is found to be lower than the minimum forced ventilation flow rate (5.57 l/s), but higher than the minimum forced flow rate at higher speeds (Fr = 1.361, 1.458) (see cyan coloured data points in Figs. 18 and 19).

Looking at the iso-speed resistance curves, two regions can be identified. The first one is characterized by drag decreasing with increasing airflow and the second one where further air flow rate increase results only in a marginal resistance reduction (Fig. 19). Overall, the trends in Figs. 18 and 19 show a significant speed dependency.

The resistance reduction depends on the wetted surface reduction due to the growing air layer, and its influence on running attitude due to the modification of the pressure distribution on the hull bottom. Varying the flow rate, the resistance reaches a constant value once the air layer is fully developed. From the plots in Figs. 18 and 19, the flow rate beyond which the resistance reaches a constant value (with negligible reductions compared to the DIS No-Air case) is 9.7 l/s.

The ineffectiveness of high flow rates is evident observing that also the running attitude (trim and CG rise) for flow rates beyond Q = 9.7 l/s (Fig. 20) remains unvaried.

In particular, it can be seen that.

- For all speeds and for flow rates above Q = 9.7 l/s, the hull running attitude is no longer affected by increasing air flow rate, leading to the resistance plateau described above.
- For low flow rates (Q < 9.7 l/s), the air injection effects on running trim and CG rise are speed dependent, indeed, at low speed (Fr = 0.972), the running trim and CG rise shows a weaker dependency on flow rate respect the cases at high speed (see cases at Fr = 1.361 and Fr = 1.458 in Fig. 20)

The comparison between computational and experimental resistance is shown in Fig. 21. The resistance obtained with numerical simulations systematically underestimates the experimental results, where the biggest differences occur for higher flow rates at high speed (Q = 15.53 and 20.47 l/s at Fr = 1.361 and 1.458).

This behavior may be due to assuming a constant density air flow.

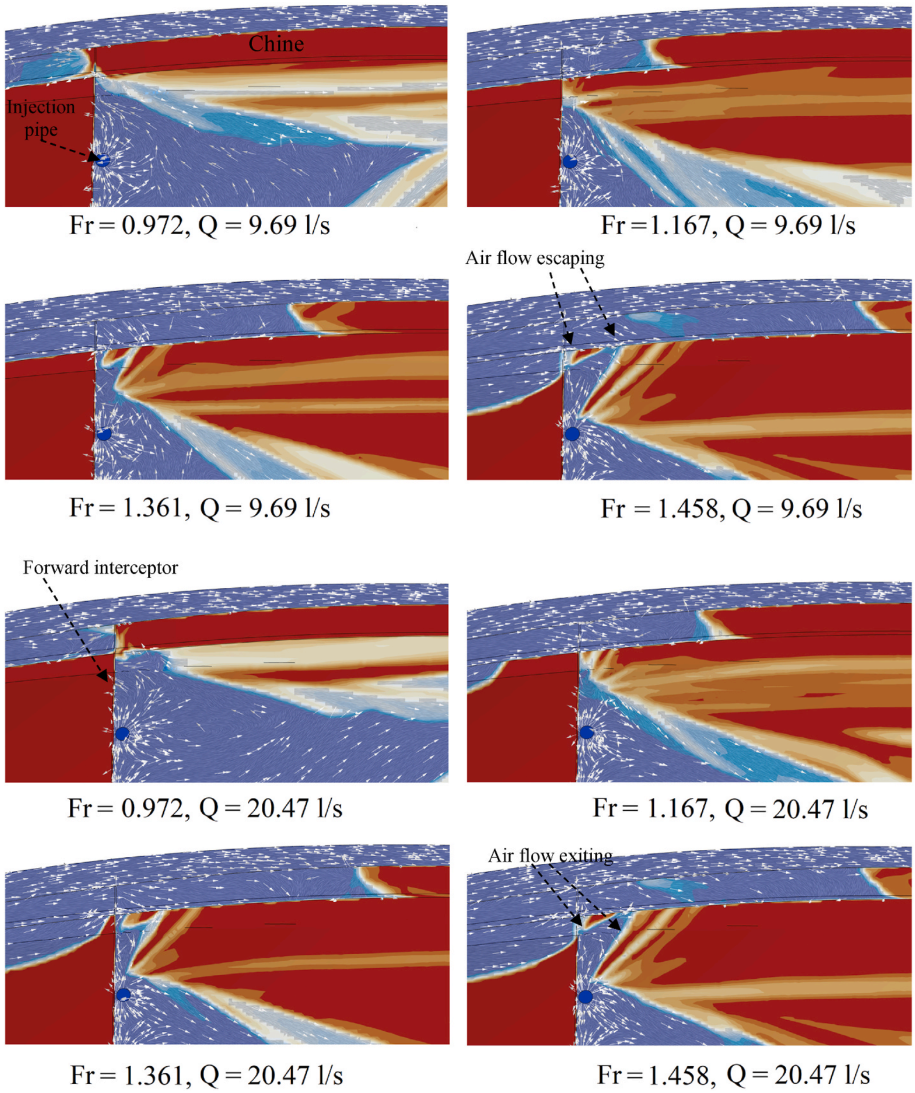

Fig. 22. Comparison of VOF and air flow vector field (white arrows) near the forward interceptor.

While this assumption may be acceptable at low airflow speeds, it becomes weaker when the air flow rate and hull speeds significantly increase, resulting in a significant increase in the local airflow velocity at the pipe outlets. However, this aspect will be further investigated in future studies.

In conclusion, the growth of the air layer is described showing volume fraction images with air vector fields obtained from CFD simulations. The CFD images can be compared to the underwater photos provided in Appendix B.

In Fig. 23, the water volume fraction for all tested conditions is shown from left to right the evolution of the dry area with increasing speed for a given flow rate, while from top to down the figure shows the dry area change with increasing air flow rate for a given boat speed.

Focusing on the cases at Q = 9.7 and 20.5 l/s, detailed images of the forward interceptor zones are reported for each speed (Fig. 22). At low speed, the overpressure generated by the flow reattachment over the chines (near the forward interceptor) does not allow the air to escape laterally with respect to the forward interceptor. Instead, the injected air vents towards the aft quarters creating two diverging tails flowing downstream. As the speed increases, the tails of the air cavity tend to move closer to the centerline and become unstable due to the overpressure zone generated by the stern interceptor. In addition, the flow reattachment on the chines moves aft, enabling the air cavity to vent mainly from the sides near the forward interceptor.

6. Conclusions & further works

In this study, the authors investigated the use of air lubrication to improve the effectiveness of the Double Interceptor System for a heavily loaded planing hull. The hull is characterized by a low L/B and $L/\nabla^{1/3}$ value (L/B = 2.55, $L/\nabla^{1/3}$ = 4.82). The work was carried out by combining experimental tests and CFD simulations. The experiments were conducted in the LEIN towing tank of the *Università degli Studi di Napoli "Federico II"*. The air lubrication technique involved ventilating the bottom hull bottom using 8 pipes installed behind the forward interceptor. Two ventilation approaches were considered, natural

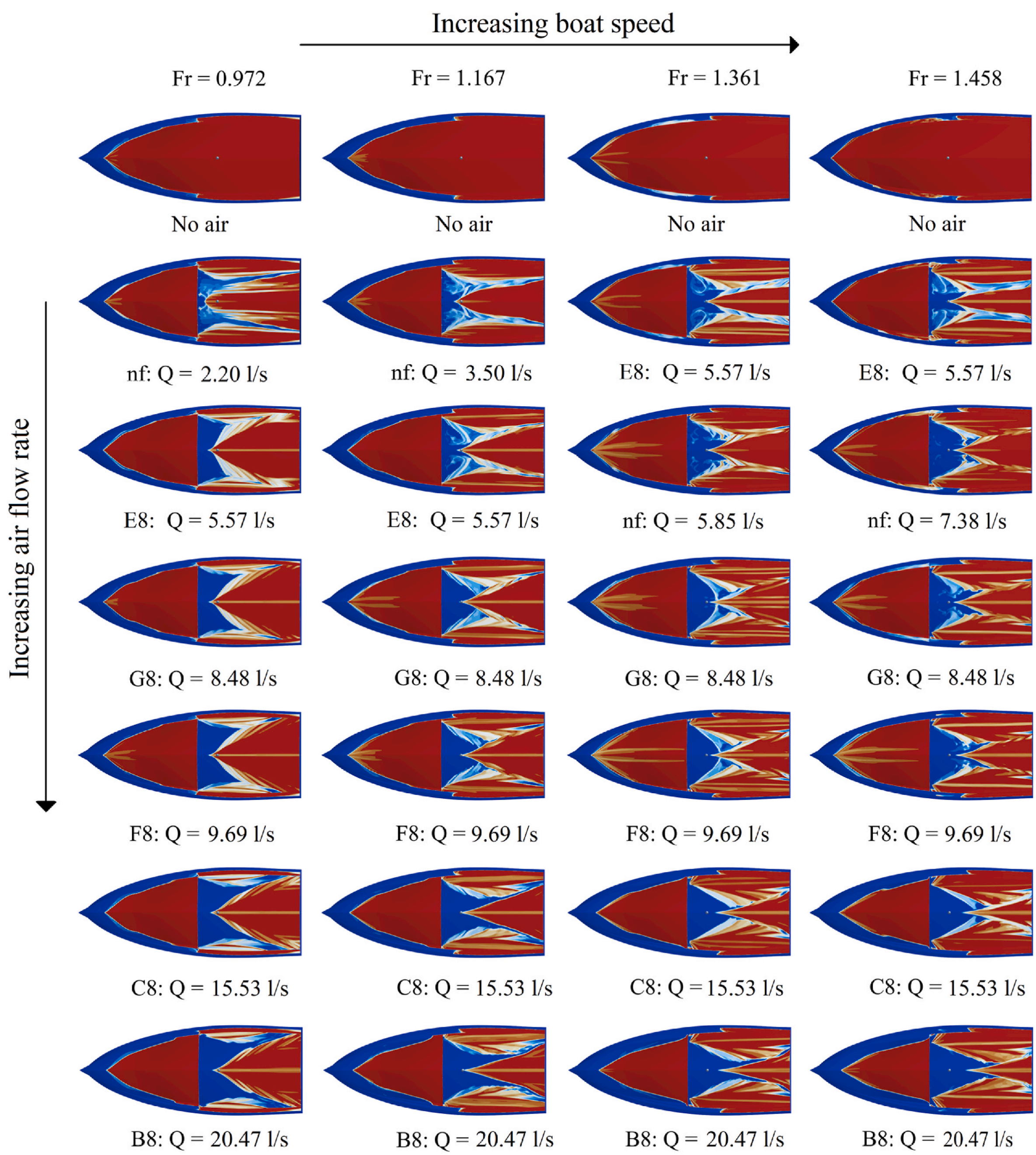

Fig. 23. Air layer development with speed and flow rate.

ventilation with open pipes subjected only to atmospheric pressure and forced ventilation using a high-pressure compressor. The model was tested at the speeds of 4.60, 5.52, 6.44, and 6.90 m/s, corresponding to Froude numbers between 0.97 and 1.46 (Fr_∇ between 0.67 and 0.94). The air flow rate range systematically varied from 0 to 20.5 l/s. The study starts with the performance analysis of the hull equipped with the non-ventilated DIS compared to the bare hull case.

It has been experienced that without proper ventilation, the low-pressure area caused by the flow separation downstream of the forward interceptor leads to excessive downforce, which penalizes its lifting capabilities. As a result, there is a reduced trim and CG rise, resulting in a larger wetted surface leading to higher shear force components compared to the bare hull case. This effect becomes more pronounced as speed increases.

The method employed to improve the ventilated DIS performance was to force the DIS ventilation through dedicated pipes placed downstream of the forward interceptor. Therefore, the analysis proceeded with experimental and numerical tests of the DIS assisted by natural and forced ventilation, resulting in a significant overall improvement compared to the non-ventilated DIS. When compared to the bare hull, the natural ventilation configuration showed some improvements in resistance at lower speeds (−10.9% and −3.1% at Fr = 0.972 and 1.167 respectively), but it was not enough to achieve substantial performance gains for higher speeds where high forced air flow rates were necessary. To achieve a resistance improvement with respect to the bare hull over the entire speed range, a minimum forced airflow rate of 9.7 l/s was required. Specifically, at low speeds (Fr = 0.972), an air flow rate of Q = 9.7 l/s corresponds to the maximum resistance reduction of 12.4% compared to the bare hull, while at high speeds (Fr = 1.458) a maximum resistance reduction of 1.2% was achieved with the highest airflow rate of Q = 20.47 l/s.

The performance improvements can be explained by analyzing the effects of ventilation on the hull dynamics, i.e. the mutual effects between the wetted surface, the pressure distribution, and the running attitude. Firstly, the ventilation led to a significant reduction of the wetted surface resulting in a decrease of shear resistance.

Secondly, the injected air modified the pressure distribution, eliminating the low-pressure zone observed downstream of the forward interceptor. Those actions led to an enhancement of DIS's lifting capability resulting in an increase in trim and hull rise, which contributed to the reduction of the wetted surface. Following this, the study continued by analyzing the influence of air flow rate on the dynamics of the DIS-equipped hull. By analyzing the hull resistance and running attitude at varying flow rates through iso-speed curves, two key regions were identified. In the first region, drag exhibits a significant decrease as airflow is progressively increased. This suggests a strong dependence between drag and airflow at lower flow rates (up to Q = 9.7 l/s). Indeed, at lower flow rates the influence of airflow on trim and CG rise is more speed dependent.

In the second region, further increases in airflow (for flow rates higher than Q = 9.7 l/s) result in only marginal reductions in resistance. This is consistent with the observation that trim, and CG rise remain almost constant for flow rates exceeding this value (Q = 9.7 l/s).

Concerning pressures, DIS-no Air increases pressure resistances due to the over-submerging of the bow.

In regard to experimental and numerical comparisons, it was found that the resistance obtained through numerical simulations consistently underestimated the experimental results, especially at higher speeds and flow rates (see Appendix A). Besides the typical source of errors in the numerical setup (grid, time-step, etc.), a further potential source may be identified in the physical models/assumptions in the simulations, such as the constant density model for forced air flow. This assumption becomes less valid at higher airflow speeds, and further studies are needed to understand the potential improvement of using different physical models for air flow as the compressibility effects become more significant.

CRediT authorship contribution statement

Vincenzo Sorrentino: Writing – review & editing, Writing – original draft, Visualization, Methodology, Investigation, Formal analysis, Data curation, Conceptualization. **Riccardo Pigazzini:** Writing – review & editing, Writing – original draft, Visualization, Methodology, Investigation, Formal analysis, Data curation, Conceptualization. **Fabio De Luca:** Writing – review & editing, Writing – original draft, Visualization, Resources, Methodology, Investigation, Formal analysis, Data curation. **Simone Mancini:** Writing – review & editing, Writing – original draft, Software, Methodology, Investigation, Formal analysis, Data curation, Conceptualization. **Claudio Pensa:** Writing – review & editing, Writing – original draft, Supervision, Resources, Project administration, Methodology, Investigation, Funding acquisition, Formal analysis, Conceptualization.

Declaration of competing interest

The authors declare that they have no known competing financial interests or personal relationships that could have appeared to influence the work reported in this paper.

Acknowledgement

The funded project PRIN 2017 - 2017X7Z8S3 “LUBRI-SMOOTH” is acknowledged for the financial support of the present work.

Appendix A. Supplementary data

Supplementary data to this article can be found online at https://doi.org/10.1016/j.oceaneng.2024.120135.

Appendix A. Experimental and Numerical Comparisons

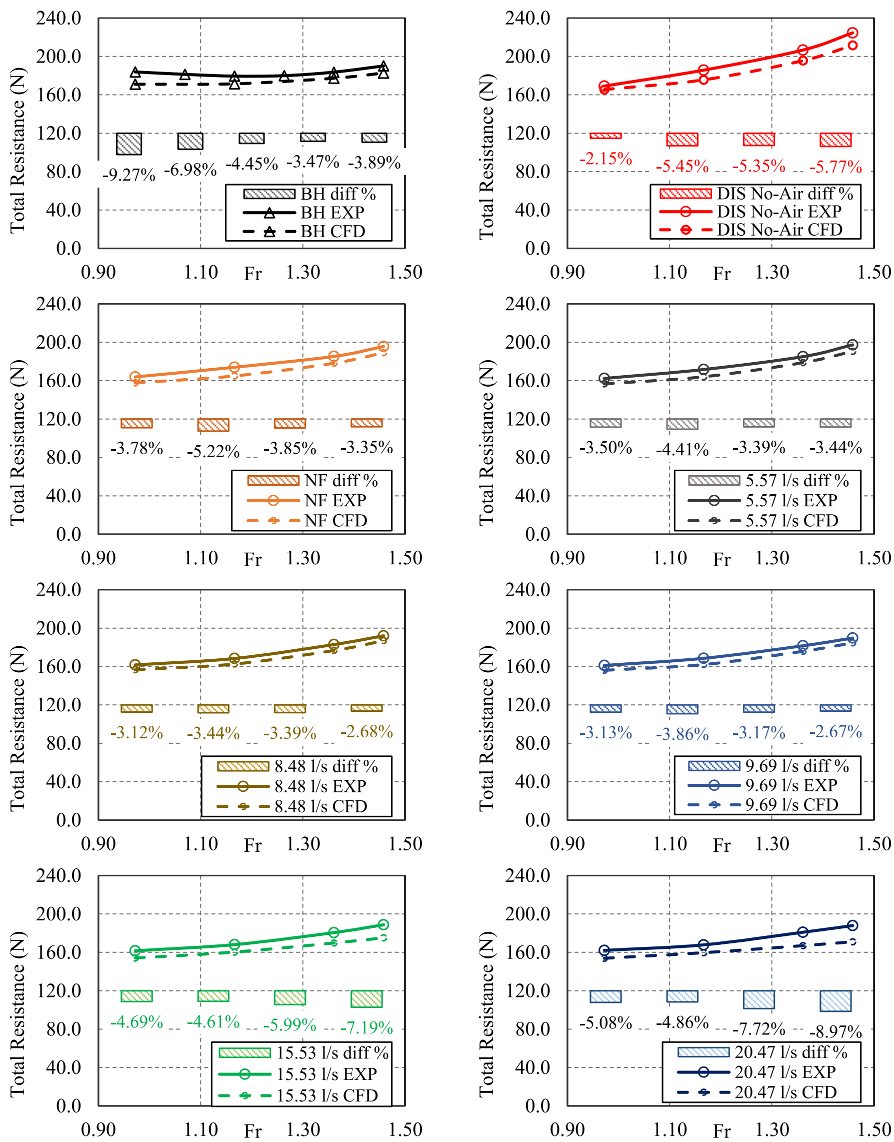

Fig. A1. Total Resistance, experimental and numerical comparisons.

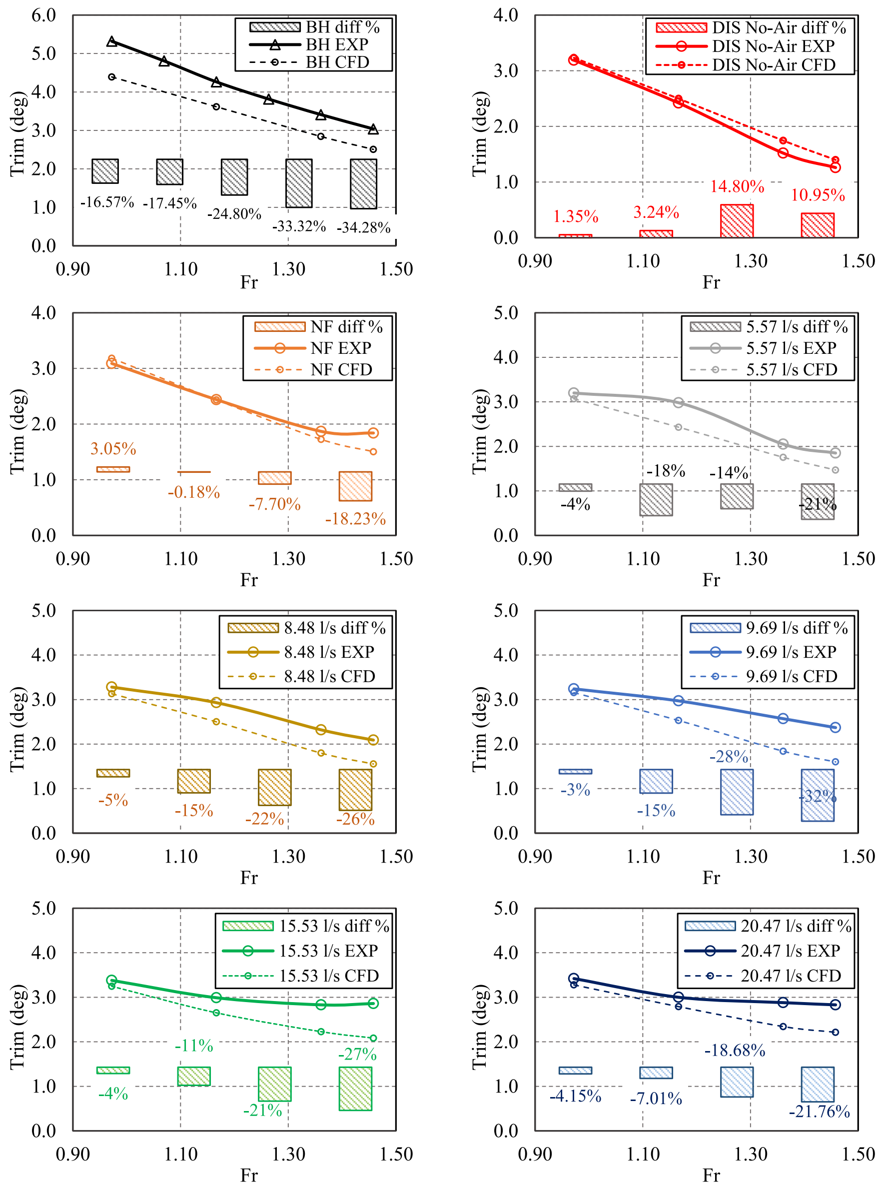

Fig. A2. Trim, experimental and numerical comparisons.

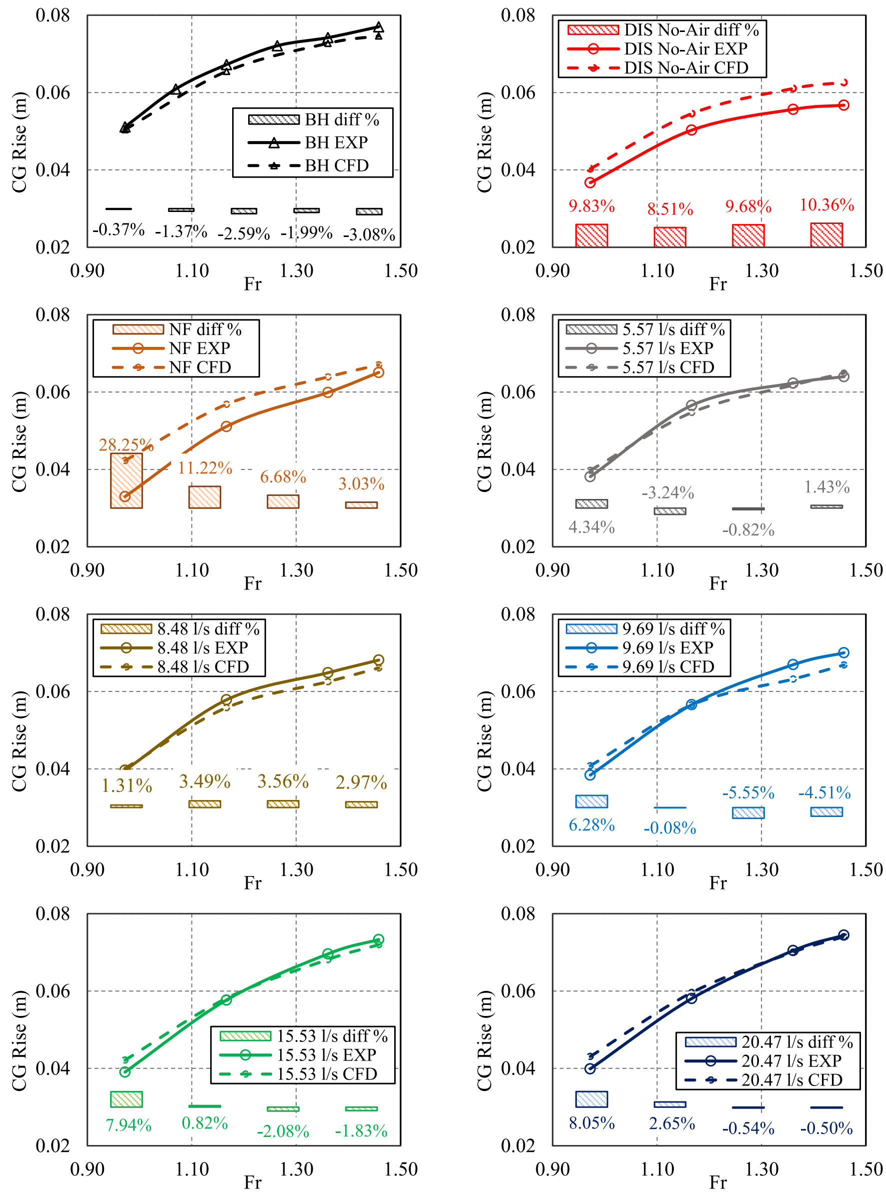

Fig. A3. CG Rise, experimental and numerical comparisons.

Appendix B. Underwater images

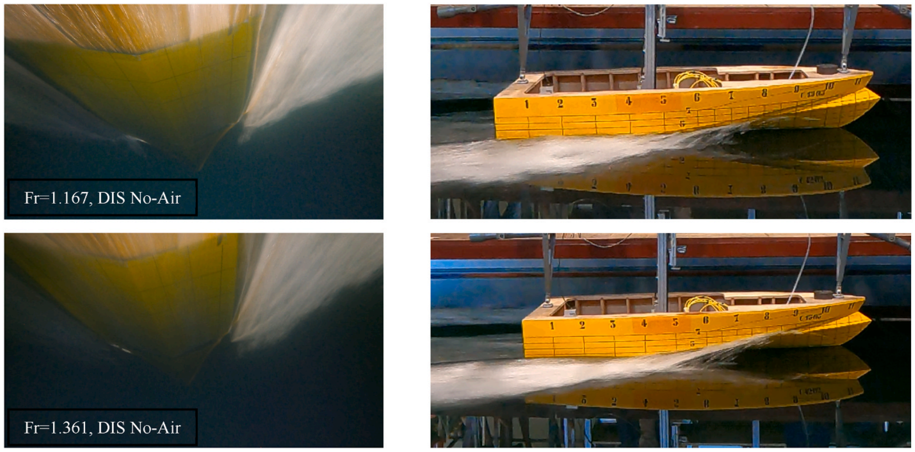

Fig. B1. Towing tank tests images for DIS No-Air cases, Fr = 1.167 and Fr = 1.361 (Underwater and side photos).

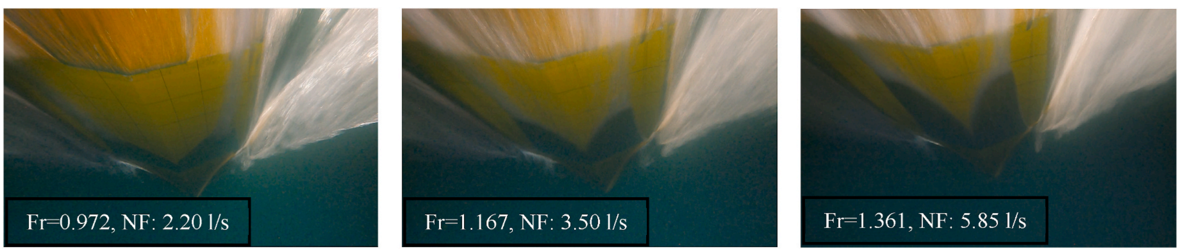

Fig. B2. Towing tank tests images for Natural Flow cases (NF) at different speeds (Underwater photos).

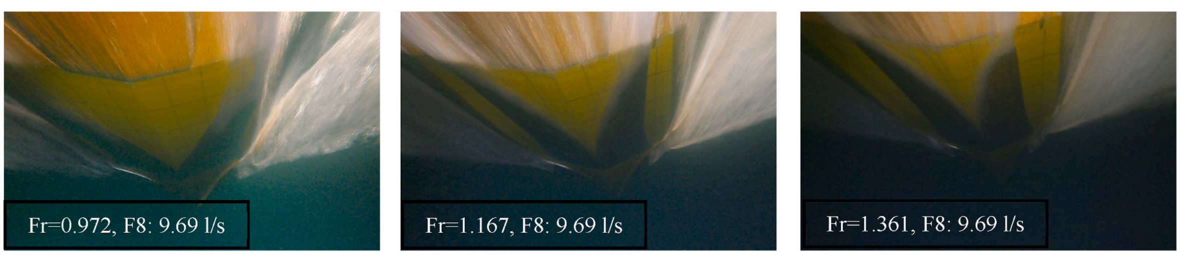

Fig. B3. Towing tank tests images for F8 case (Q = 9.69 l/s) at different speeds (Underwater photos).

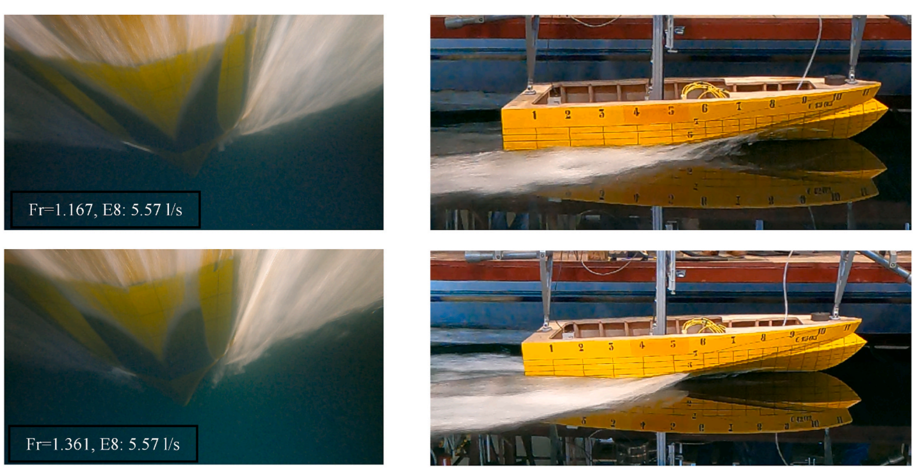

Fig. B4. Towing tank tests images for E8 case (Q = 5.57 l/s), Fr = 1.167 and Fr = 1.361 (Underwater and side photos).

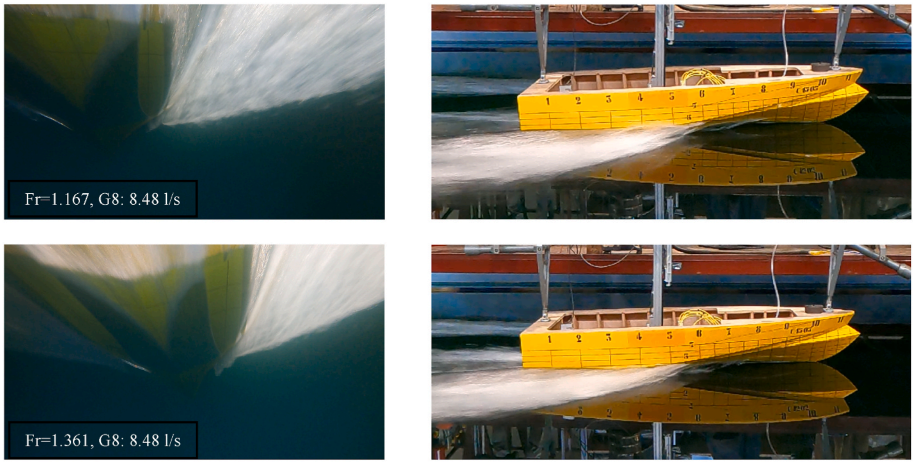

Fig. B5. Towing tank tests images for G8 case (Q = 8.48 l/s), Fr = 1.167 and Fr = 1.361 (Underwater and side photos).

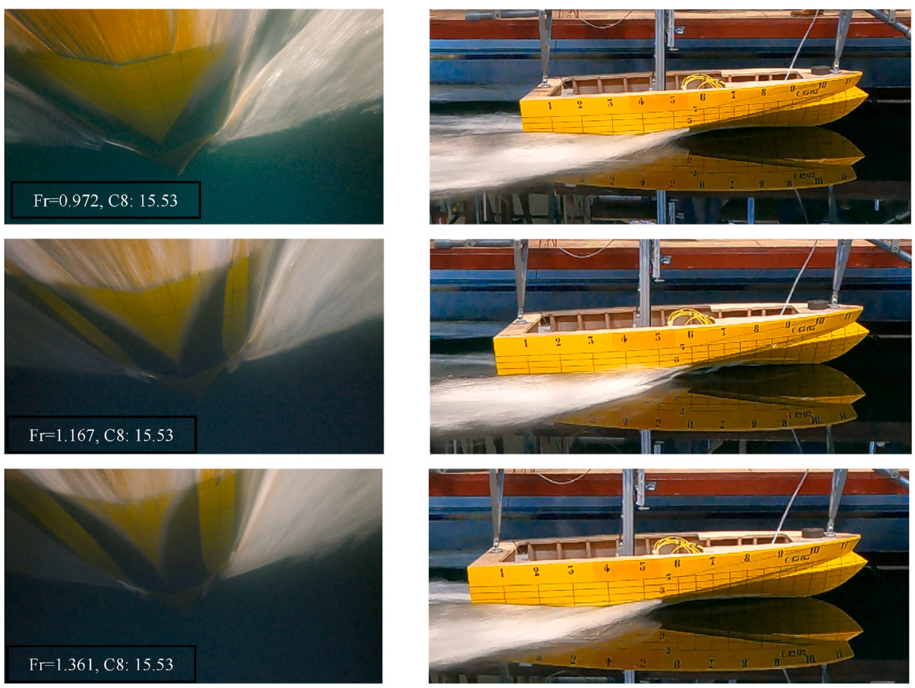

Fig. B6. Towing tank tests images for G8 case (Q = 8.48 l/s), Fr = 0.972, Fr = 1.167 and Fr = 1.361 (Underwater and side photos).

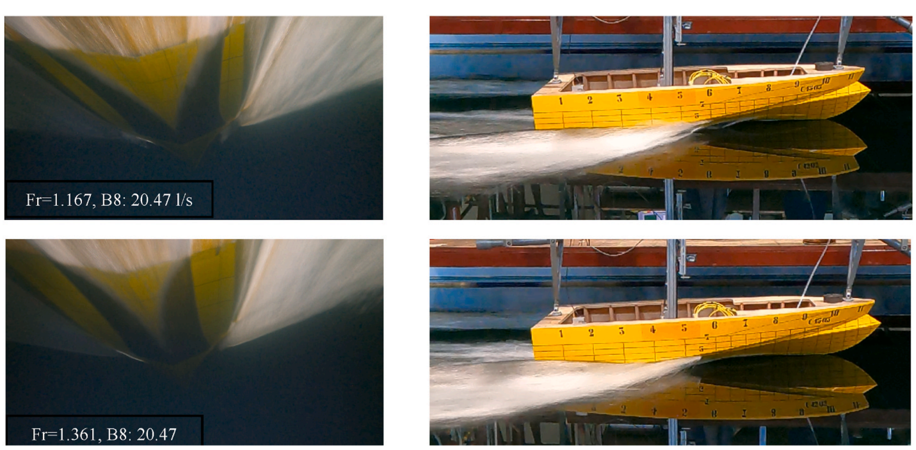

Fig. B7. Towing tank tests images for B8 case (Q = 20.47 l/s), Fr = 1.167 and Fr = 1.361 (Underwater and side photos).

References

An, H., Pan, H., Yang, P., 2022. Research progress of air lubrication drag reduction Technology for ships. Fluids 7 (10), 319.

Butuzov, A.A., 1966. Limiting parameters of an artificial cavity formed on the lower surface of a horizontal wall. Fluid Dynam. 1 (2), 116–118.

Collins, J.M., Whitworth, P.R., Matveev, K.I., 2021. Experimental testing and numerical modeling of small-scale boat with drag-reducing air-cavity system. In: Fluids Engineering Division Summer Meeting, vol. 85307. American Society of Mechanical Engineers, V003T08A008.

De Luca, F., Mancini, S., Miranda, S., Pensa, C., 2016. An extended verification and validation study of CFD simulations for planing hulls. J. Ship Res. 60 (2), 101–118.

De Luca, F., Mancini, S., Pensa, C., Pigazzini, R., Sorrentino, V., 2022. A DIS-based air cavity Concept for planing hull. In: Technology and Science for the Ships of the Future. IOS Press, pp. 538–545.

De Luca, F., Pensa, C., 2012a. Experimental investigation on conventional and Unconventional interceptors. The Transactions of International Journal of Small Craft Technology 154. Part B2 Jul-Dec 2012.

De Luca, F., Pensa, C., 2012b. Unconventional interceptors in still water and in regular Waves: experimental study on resistance reduction and dynamic instability. In: 17th International Conference on Ships and Shipping Research 2012. NAV 12, Naples 17-19 October.

De Luca, F., Mancini, S., Pensa, C., Pigazzini, R., Sorrentino, V., 2023a. Full-scale CFD simulations of air lubrication with DIS-based air cavity for planing hull. In: Marine, 2023.

De Luca, F., Mancini, S., Pensa, C., Pigazzini, R., Sorrentino, V., 2023b. Experimental investigation on the effect of single and double interceptor systems on planing hull efficiency with different loading conditions. In: Conference: 4th International Naval Architecture and Maritime Symposium (INT-NAM 2023).

Elbing, B.R., Winkel, E.S., Lay, K.A., Ceccio, S.L., Dowling, D.R., Perlin, M., 2008. Bubble-induced skin-friction drag reduction and the abrupt transition to air-layer drag reduction. J. Fluid Mech. 612, 201–236.

Fang, H., Qin, S., Sun, S., Wang, L., Feng, X., Huang, B., Wu, D., 2021. Numerical investigation on the cavity behavior and hydrodynamic performance of a planing air cavity ship. Ocean Engineering 241, 110042.

Fang, H., Chen, Z., Chen, C., Sun, S., Wang, X., Wu, D., Qin, S., 2023. On the drag reduction and heeling stability of a heeled planing air cavity hull. Ocean Engineering 283, 115087.

IMO, 2023. IMO strategy on reduction of GHG emissions from ships. MEPC 377 (80), 7 July 2023.

International Towing Tank Conference (ITTC), 2014. Recommended Procedures and Guidelines 7.5-03 02-03 – Practical Guidelines for Ship CFD Applications.

Kumagai, I., Takahashi, Y., Murai, Y., 2015. Power-saving device for air bubble generation using a hydrofoil to reduce ship drag: Theory, experiments, and application to ships. Ocean Engineering 95, 183–194.

Latorre, R., 1997. Ship hull drag reduction using bottom air injection. Ocean engineering 24 (2), 161–175.

Latorre, R., Miller, A., Philips, R., 2002. Microbubble resistance reduction for high-speed craft. SNAME Transactions 110, 259–277.

Mc Cormick, M.E., Bhattacharyya, R., 1973. Drag reduction of a submersible hull by electrolysis. Nav. Eng. J. 85 (2), 11–16.

Matveev, K.I., 2003. On the limiting parameters of artificial cavitation. Ocean Engineering 30 (9), 1179–1190.

Matveev, K.I., Burnett, T.J., Ockfen, A.E., 2009. Study of air-ventilated cavity under model hull on water surface. Ocean Engineering 36 (12–13), 930–940.

Ricks, A., Morabito, M.G., Datla, R., 2023. Effect of ventilation on cavity formation on stepped planing hulls. J. Ship Res. 67 (1), 32–47.

Sanders, W.C., Winkel, E.S., Dowling, D.R., Perlin, M., Ceccio, S.L., 2006. Bubble friction drag reduction in a high-Reynolds-number flat-plate turbulent boundary layer. J. Fluid Mech. 552, 353–380.

Stern, F., Wilson, R.V., Coleman, H.W., Paterson, E.G., 2001. Comprehensive approach to verification and validation of CFD simulations - Part 1: methodology and Procedures. J. Fluid Eng. 123, 793–802.

Siemens PLM Star-CCM+ V. 2022.1.1 User's Guide, 2022. Siemens.

Tanaka, T., Oishi, Y., Park, H.J., Tasaka, Y., Murai, Y., Kawakita, C., 2023. Downstream persistence of frictional drag reduction with repetitive bubble injection. Ocean Engineering 272, 113807.

Vitiello, L., Mancini, S., Bilandi, R.N., Dashtimanesh, A., De Luca, F., Nappo, V., 2022. A comprehensive stepped planing hull systematic series: Part 1-Resistance test. Ocean Engineering 266, 112242.

Wang, Z., Yang, J., Stern, F., 2010. URANS study of air-layer drag reduction in a high-Reynolds-number flat-plate turbulent boundary layer. In: In40th Fluid Dynamics Conference and Exhibit, p. 4276.

Wang, L., Huang, B., Qin, S., Cao, L., Fang, H., Wu, D., Li, C., 2020. Experimental investigation on ventilated cavity flow of a model ship. Ocean Engineering 214, 107546.